Nonaxisymmetric flow characteristics in head-on collision of spinning droplets

Chengming He (何成明) and Peng Zhang (张鹏)*
Department of Mechanical Engineering, The Hong Kong Polytechnic University, Hung Hom, Kowloon 999077, Hong Kong

(Received 10 June 2020; accepted 13 October 2020; published 2 November 2020)

The effects of spinning motion on the bouncing and coalescence between a spinning droplet and a nonspinning droplet undergoing head-on collision were numerically studied by using a volume-of-fluid method. A prominent discovery is that the spinning droplet can induce significant nonaxisymmetric flow features for the head-on collision of equal-size droplets composed of the same liquid. Specifically, a nonaxisymmetric bouncing was observed, and it is caused by the conversion of the spinning angular momentum into the orbital angular momentum. This process is accompanied by the rotational kinetic energy loss due to the interaction between the rotational and radial flows of the droplets. A nonaxisymmetric internal flow and a delayed separation after temporary coalescence were also observed, and they are caused by the enhanced interface oscillation and internal-flow-induced viscous dissipation. The spinning motion can also promote the mass interminglement of droplets, because the locally nonuniform mass exchange occurs at the early collision stage by nonaxisymmetric flow and is further stretched along the filament at later collision stages. In addition, it is found that the nonaxisymmetric flow features increase with increasing the orthogonality of the initial translational motion and the spinning motion of droplets.

DOI: 10.1103/PhysRevFluids.5.113601

I. INTRODUCTION

Collision of two liquid droplets in a gaseous environment is ubiquitous in nature and industries. Many experimental studies have been reported [1–10] and reviewed [11–13] in the literature. Most of them were focused on identifying and interpreting various outcomes of droplet collision [3–5,7–9], such as coalescence, bouncing, separation, and shattering [14,15], rendering a well-known collision nomogram in the We $-$ B parameter space. The collision Weber number is $\mathrm{We} = \rho_l D_l U^2/\sigma_l$ (where ρ_l is the density of the liquid, D_l the droplet diameter, U the relative velocity, and σ_l the surface tension), which measures the relative importance of the droplet inertia compared to the surface tension, and the impact parameter is $B = \chi/D_l$ (where χ is the projection of two mass centers connection line in the direction perpendicular to U), which measures the deviation of the trajectory of droplets from that of the head-on collision, with $B = 0$ denoting the head-on collision and $B = 1$ the grazing collision. In addition, the influences of some other controlling parameters on the collision outcomes have also been investigated, such as the droplet Ohnesorge number [7,9,16,17], $\mathrm{Oh} = \mu_l/\sqrt{\rho_l D_l \sigma_l}$ (where μ_l is the dynamic viscosity of the liquid), which measures the relative importance of the liquid viscous stress compared to the capillary pressure, and the size ratio [3,18–20] Δ, which measures the droplet size disparity. In addition, the collision outcomes can be significantly affected by the gas environment, as increasing the gas pressure promotes droplet bouncing and decreasing the gas pressure promotes droplet coalescence [4,5].

*Author to whom correspondence should be addressed: pengzhang.zhang@polyu.edu.hk

 ©2020 American Physical Society

A practical significance of the gas pressure effect is that colliding fuel droplets may tend to bounce off under high pressure in real combustion chambers, and this has been verified both experimentally and numerically [21–23].

It has been recognized that the colliding droplets usually have a spinning motion. The spinning motion can be created either from droplet injectors (by nonuniform driving pressure) or from preceding collisions, which are off-center as a large probability. Bradley and Stow [2] showed the experimental images of droplet spin after coalescence and measured the angle of rotation as a function of time and impact parameter. Ashgriz and Poo [3] proposed the schematic of reflexive separation for the off-center droplet collision by considering the droplet spin after coalescence. Rotational energy [4,6] has been considered in various models for predicting outcomes of off-center droplet collisions. However, the fact that the spinning motion of a droplet after off-center collisions can take part of the energy from its translational motion has not been considered in the previous models. It is noted that the spinning droplets can collide with each other, because subsequent collisions are highly probable in practical dense sprays [21,24,25], but relevant studies have not been seen in the literature.

The spinning effects on a single droplet have been investigated by a number of studies. Brown and Scriven [26] used a finite-element method to trace the equilibrium state of axisymmetric, two-, three-, and four-lobed drop shape for rotating droplets and analyzed the critical transition between different drop shapes. Kitahata *et al.* [27] proposed a simple mechanical model to measure the liquid surface tension by use of the frequency-amplitude relation of oscillation of a levitated rotating droplet. Holgate and Coppins [28] numerically studied the equilibrium shapes and stability of rotating charged drops in a vacuum and proposed a formula for stability limit. The phenomena of droplet distortion and spinning can be further enriched by the involvement of rotating environmental flows [29,30] or external fields [31].

In this paper we shall present a computational study on the collision of spinning droplets. This study restricts its scope to the head-on collision between droplets of equal size so as to avoid unnecessary complexity of geometrical asymmetry and size disparity, which certainly merit future studies. Furthermore, the ideally spherical shape of droplets is assumed before their collision, because the characteristic rotational energy, $M_l\Omega^2 D_l^2/4$ (where M_l and Ω are the dimensional mass and angular velocity of the droplet), due to the droplet spinning motion is substantially smaller than the surface energy, $\pi\sigma_l D_l^2$, with the ratio $M_l\Omega^2/4\pi\sigma_l$ being $O(10^{-1})$ or less (see the following section for the estimation of angular velocity Ω). Consequently, the spinning droplet is negligibly deformed due to its centrifugal force. The presentation of the study is organized as follows. The numerical methodology and specifications are described in Sec. II. The results of the bouncing and coalescence between a spinning droplet and a nonspinning droplet are presented in Secs. III and IV, respectively.

II. NUMERICAL METHODOLOGY AND SPECIFICATIONS

A. Numerical method

The three-dimensional continuity and incompressible Navier-Stokes equations,

$$\nabla \cdot \boldsymbol{v} = 0, \tag{1}$$

$$\rho(\partial \boldsymbol{v}/\partial t + \boldsymbol{v} \cdot \nabla \boldsymbol{v}) = -\nabla p + \nabla \cdot (2\mu \boldsymbol{D}) + \sigma\kappa \boldsymbol{n}\delta_s, \tag{2}$$

are solved by using the classic fractional-step projection method, where $\boldsymbol{v}$ is the velocity vector, ρ the density, p the pressure, μ the dynamic viscosity, and $\boldsymbol{D}$ the deformation tensor defined as $D_{ij} = (\partial_j u_i + \partial_i u_j)/2$. In the surface tension term $\sigma\kappa\boldsymbol{n}\delta_s$, δ_s is a Dirac delta function, σ the surface tension coefficient, κ the local curvature, and the unit vector $\boldsymbol{n}$ normal to the local interface.

To solve both the gas and liquid phases, the density and viscosity are constructed by the volume fraction as $\rho = c\rho_l + (1-c)\rho_g$ and $\mu = c\mu_l + (1-c)\mu_g$, in which the subscripts l and g denote

the liquid and gas phases, respectively. The volume fraction c satisfies the advection equation,

$$\partial c/\partial t + \nabla \cdot (c\boldsymbol{v}) = 0, \tag{3}$$

with $c = 1$ for the liquid phase, $c = 0$ for the gas phase, and $0 < c < 1$ for the gas-liquid interface. The present study simulating droplet collisions adopts the volume-of-fluid (VOF) method, which has been implemented in the open source code, GERRIS [32,33], featuring the three-dimensional octree adaptive mesh refinement, the geometrical VOF interface reconstruction, and continuum surface force with height function curvature estimation. GERRIS has been demonstrated to be competent for solving a wide range of multiphase flow problems [19,34–40].

A major challenge of VOF simulations on droplet collision lies in the inability of the Navier-Stokes equations in describing the rarified gas effects and the van der Waals force [41] within the gas film, thereby prohibiting the physically correct prediction of droplet coalescence. A coarse mesh would induce "premature" coalescence of the droplets that realistically bounce off. Thus the successful simulation of droplet coalescence and subsequent collision dynamics in previous studies [19,20,34–36] were obtained by choosing an appropriate mesh resolution near the interface. Similarly, the conventional VOF simulation on droplet bouncing requires an extremely refined mesh and a substantial computational cost; we thereby adopted two VOF functions [37,38,42] to separately track the interface of each liquid droplet so as to avoid interface coalescence on a relatively coarse mesh. The method with two VOF functions was successfully applied to study droplet bouncing and has been verified by experiments. It can produce nearly the same droplet deformation and minimum interface distance for droplet bouncing cases compared to the conventional VOF approach. Furthermore, the droplet interfaces can be advected in the two immediately neighboring interface cells, leading to the minimum interface distance being smaller than the minimum mesh size. More details about the two VOF methods and their comparison have been sufficiently discussed in the literature [37,38,42].

B. Numerical validations

In this work we investigated a few important droplet collision phenomena, such as droplet bouncing, coalescence, separation, and internal mass interminglement. Among these phenomena, droplet bouncing requires additional numerical treatment in order to balance computational accuracy and cost. We thereby used two VOF functions for the bouncing cases and the one VOF function for other cases. Furthermore, to improve computational efficiency, the computational domain is divided into three physical zones, namely, the gas, the droplet, and the interface, and each zone has its own mesh refinement level denoted by N, which corresponds to a minimum mesh size of $O(2^{-N})$. Accordingly, (N_g, N_d, N_i) is used to describe the refinement level in the three zones.

First, the head-on droplet bouncing was simulated and compared with the experimental results of Pan *et al.* [10]. The approach of two VOF functions with a mesh refinement level of (3, 5, 7) was used as a balance between computational cost and accuracy. The numerical validations and grid independence analysis were conducted in our previous studies [37]. Given the maximum mesh refinement level $N_i = 7$ in the interface zone, the maximum numerical resolution (MNR) [38] for a droplet can be defined as $\mathrm{MNR} = 2^{N_i} + 1 = 129$, which means there are 129 grid points per droplet diameter if the same refinement level is also applied to the droplet zone. In practice, $N_d = 5$ in the droplet zone is adequate to characterize the details of the droplet interior flow, and the total grid points per droplet diameter is thereby less than the MNR. A typical simulation run with the mesh refinement level (3, 5, 7) results in 4.8×10^5 grid points in the entire droplet, which is equivalent to about 4.3×10^6 grid points if applying a uniform mesh with size of $O(2^{-7})$. It takes about 100 hours of real time to run the simulation up to $T = 2.0$ on an Intel Xeon(R) E5-2630 processor with 16 cores.

Second, the head-on droplet coalescence was simulated by using the conventional VOF method with a mesh refinement level of (4, 7, 8). The numerical validations and grid independence analysis were conducted by Chen *et al.* [34]. The droplet coalescence at $\mathrm{We} = 61.4$ and $\mathrm{Oh} = 2.80 \times 10^{-2}$

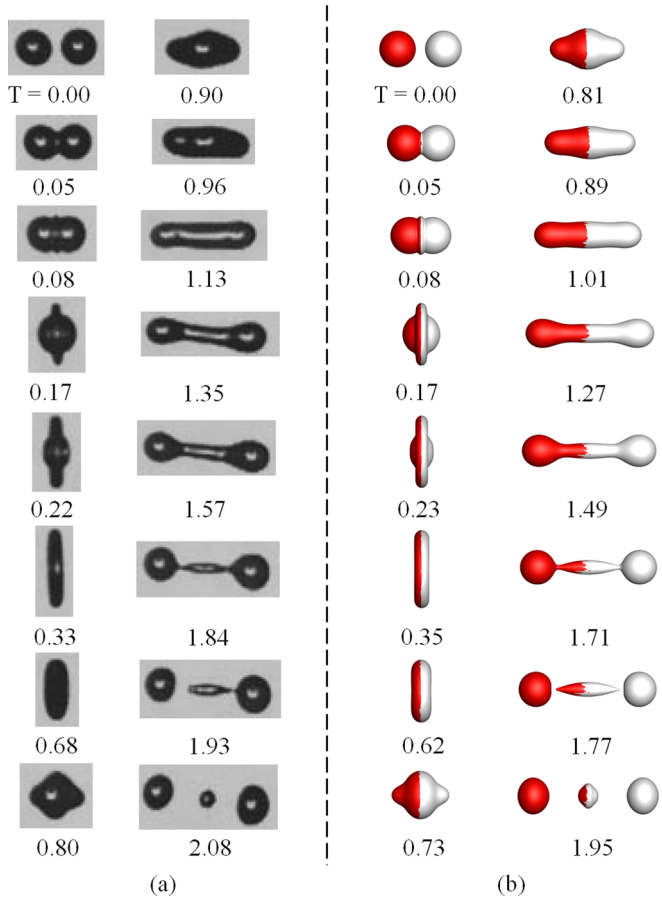

FIG. 1. Comparison of (a) experimental images adapted from Qian and Law [5] and (b) the present numerical results for the head-on coalescence of identical droplets at We = 61.4 and Oh = 2.80×10^{-2}. The dimensionless time $T = t/t_{\text{osc}}$ and $t_{\text{osc}} = 1.06$ ms.

was reproduced and compared with the experimental images from Qian and Law [5] in Fig. 1. The nondimensional time is defined as $T = t/t_{\text{osc}}$, where t is the physical time and $t_{\text{osc}} = \sqrt{\rho_l {D_l}^3/\sigma_l}$ the characteristic oscillation time. The experimental and simulation times are nearly the same in early collision stages and begin to show slight discrepancies as time evolves in later stages. The time errors are generally less than 8%. A typical simulation run with the mesh refinement level (4, 7, 8) results in MNR = 257 and 3.73×10^6 grid points in the entire droplet, taking about 200 hours of real time to run the simulation up to $T = 2.0$ on two Intel Xeon(R) Gold-6150 processors with 72 cores (36 cores for each processor).

C. Evaluation of droplet spinning speed

A key process in setting up the initial conditions for the present simulations is to specify the physically realistic spinning speed of droplets. It has not been seen in the literature on the experimental measurement of the spinning speed of droplets after collisions, probably because of the difficulty of experimentally resolving the droplet spinning motion under the sub-mini scales of length and time. Consequently, we analyzed the simulation data in the literature [37] to evaluate the

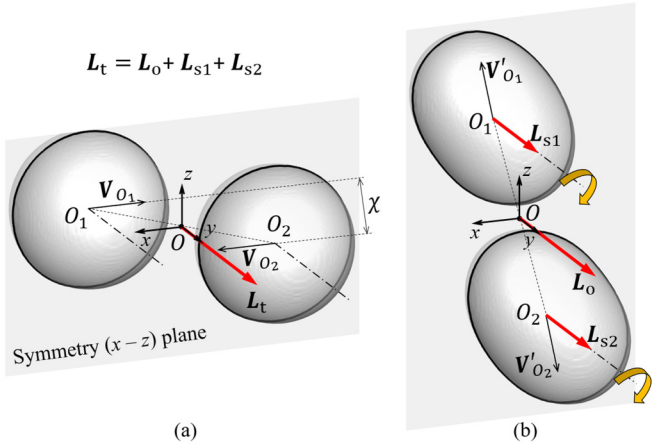

FIG. 2. Schematic of arbitrary off-center droplet collision involving a symmetry (x-z) plane and conservation of angular momentum (a) before and (b) after the collision, in which $\boldsymbol{L}_t$, $\boldsymbol{L}_o$, $\boldsymbol{L}_{s1}$, and $\boldsymbol{L}_{s2}$ are the total, orbital, and spinning (subscript "1" and "2" denote two droplets) angular momentum and have only one component in the y direction.

physically realistic range of the rotational speed for a droplet that is made to spin as the result of a preceding collision.

Figure 2 shows the general schematic of an off-center droplet collision. There always exists a symmetry (x-z) plane [37,43] that is established by the x axis and the connection line O_1O_2 (hereinafter referred to $\overline{O_1O_2}$) of the mass centers of the colliding droplets. As the evolution of droplet deformation, the origin of the mass-center coordinate system is always located at the midpoint of $\overline{O_1O_2}$ owing to the vanishing linear momentum in the coordinate system, and the velocity vectors before and after the collision are denoted as $\boldsymbol{V}$ and $\boldsymbol{V}'$. The subscripts "O_1" and "O_2" are denoted for two droplets at each mass center, respectively. The velocity vectors are always on the symmetry plane for the head-on collision, which is a special case with the relative velocity being parallel to $\overline{O_1O_2}$.

The angular momentum $\boldsymbol{L}_o$ and $\boldsymbol{L}_s$ are shown in Fig. 2, where $\boldsymbol{L}_o$ is the orbital angular momentum with respect to the y axis, and $\boldsymbol{L}_s$ for each liquid droplet is the spin angular momentum with respect to the spinning axis across its mass center. As the evolution of droplet deformation, the position vectors $\boldsymbol{R}$ of the mass centers O_1 and O_2 for two droplets can be numerically calculated by

$$\boldsymbol{R}_{O_1} = \int_V \rho H(c_1 - 1)\boldsymbol{r}dV/M_1, \tag{4a}$$

$$\boldsymbol{R}_{O_2} = \int_V \rho H(c_2 - 1)\boldsymbol{r}dV/M_2, \tag{4b}$$

where $H(c-1)$ is the Heaviside step function which limits the integration domain to be within the droplets, $\boldsymbol{r}$ the position vector varying in space, and V the integral volume of liquid and gas phases. Consequently, $\boldsymbol{L}_o$ and $\boldsymbol{L}_s$ can be further expressed by

$$\boldsymbol{L}_o = \int_V \left[\rho H(c_1 - 1)\boldsymbol{R}_{O_1} + \rho H(c_2 - 1)\boldsymbol{R}_{O_2}\right] \times \boldsymbol{V}dV \tag{5}$$

and

$$\boldsymbol{L}_{s1} = \int_V \rho H(c_1 - 1)\left(\boldsymbol{r} - \boldsymbol{R}_{O_1}\right) \times \boldsymbol{V}dV, \tag{6a}$$

$$\boldsymbol{L}_{s2} = \int_V \rho H(c_2 - 1)\left(\boldsymbol{r} - \boldsymbol{R}_{O_2}\right) \times \boldsymbol{V}dV. \tag{6b}$$

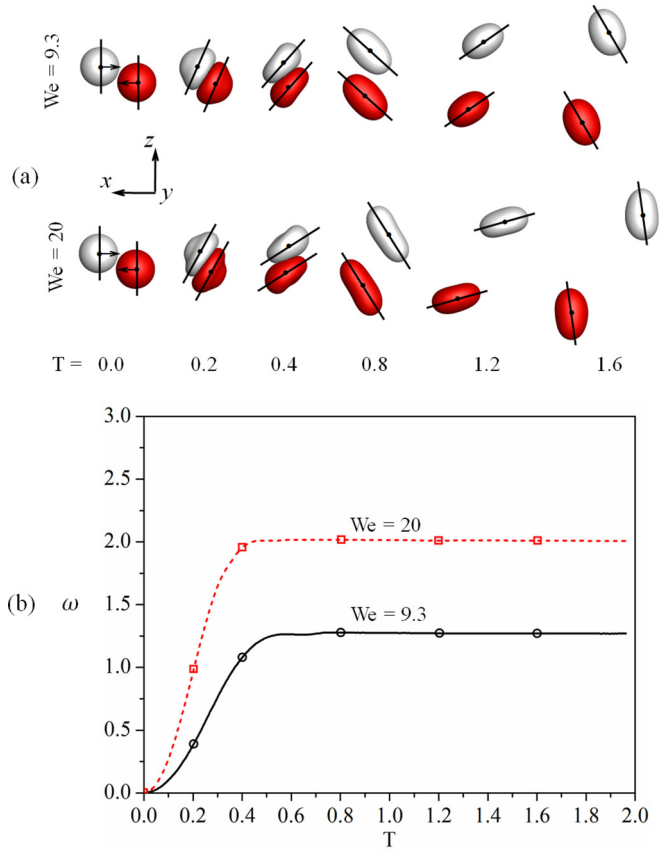

FIG. 3. Evolution of (a) droplet deformation and spinning motion and (b) nondimensional angular velocity ω for bouncing droplets at $B = 0.4$ and $\mathrm{Oh} = 2.8 \times 10^{-2}$ at $\mathrm{We} = 9.3$ and $\mathrm{We} = 20$.

Apparently, $\boldsymbol{L}_\mathrm{t}$, $\boldsymbol{L}_\mathrm{o}$, and $\boldsymbol{L}_\mathrm{s}$ vanish for head-on collisions. Whereas the off-center droplet collision has a symmetry (x-z) plane, the angular momentums have only one component in the y direction. Consequently, based on the numerical calculation of $L_{\mathrm{s}1}\boldsymbol{j}$ (same to $L_{\mathrm{s}2}\boldsymbol{j}$ owing to the symmetry), the angular velocity of droplet 1 or 2 (hereinafter referred to D1 or D2) in the y direction can be estimated by $\omega\boldsymbol{j} = L_{\mathrm{s}1}\boldsymbol{j}/I_1$, where the inertia of moment I_1 of D1 is a scalar that is numerically calculated by

$$I_1 = \int_V \rho H(c_1 - 1)\big(\boldsymbol{r} - \boldsymbol{R}_{O_1}\big)^2 dV. \tag{7}$$

The rotational deformation and spinning angular velocity of droplets are characterized in Fig. 3 by two representative cases of off-center droplet bouncing at $\mathrm{We} = 9.3$ and $\mathrm{We} = 20$, which have been discussed in detail in our previous paper [37]. As shown in Fig. 3(a), the solid point and line denote the time-dependent center of mass and the initial intersecting plane, respectively. The nondimensional angular velocity ω in Fig. 3(b) increases rapidly at the early stage from $T = 0.0$ to about 0.5 and then remains unchanged during late stages. Droplet rotation after off-center collisions favors larger We, with $\omega \approx 1.25$ for $\mathrm{We} = 9.3$ and $\omega \approx 2.0$ for $\mathrm{We} = 20$, which corresponds to dimensional angular velocities $\Omega = \omega\Omega_\mathrm{c}$ of 1886 and 1179 rad/s, respectively. Here Ω_c is the characteristic angular velocity given by $\Omega_c = 1/t_\mathrm{osc} = 943\,\mathrm{rad/s}$. Furthermore, the collision of droplets in elevated pressure environment [4,5] tends to bounce at a higher We and thereby

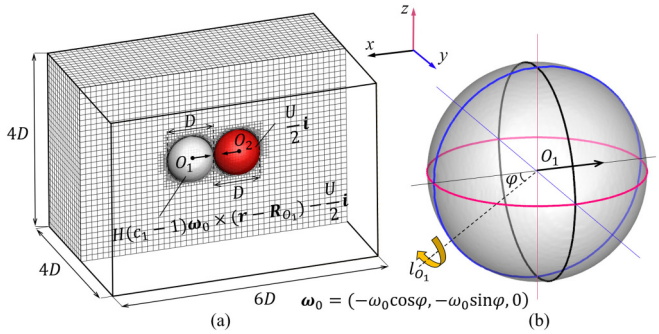

FIG. 4. Schematic of (a) three-dimensional computational domain and (b) setup of spinning axis l_{O_1} and initial velocity vector for the head-on collision between a spinning droplet 1 and a nonspinning droplet 2.

induces a stronger droplet spinning. Thus the present study adopts a range of $\omega = 1.0 \sim 3.0$, which corresponds to Ω being about $1000 \sim 3000$ rad/s.

D. Problem description and numerical specifications

The 3D computational domain of the head-on collision (with vanishing impact parameter B) between a spinning D1 and a nonspinning D2 is illustrated in Fig. 4. The spinning axis l_{O_1} of D1 can be described by a polar angle θ with respect to the z axis and an azimuthal angle φ to the x axis. In the present study the polar angle θ is fixed at $\pi/2$ and the azimuthal angle varies in the range of $0 \leqslant \varphi \leqslant \pi/2$. Then the initial spinning angular velocity can be expressed as $\boldsymbol{\omega}_0 = (-\omega_0\cos\varphi, -\omega_0\sin\varphi, 0)$.

Two droplets of diameter D are specified to collide along the x direction with a relative translational velocity U and therefore they have zero relatively velocities in the y and z directions. The translational velocity component for D1 and D2 are set as $-\frac{U}{2}\boldsymbol{i}$ and $\frac{U}{2}\boldsymbol{i}$, respectively, so that the linear momentum of the entire mass-center system remains zero. The spinning velocity components of D1 are given by $H(c_1 - 1)\boldsymbol{\omega}_0 \times (\boldsymbol{r} - \boldsymbol{R}_{O_1})$. The domain is $6D$ in length and $4D$ in both width and height, with all boundaries specified with the free outflow boundary conditions. To avoid the unnecessary complexity and to emphasize the spinning effects on the droplet collision dynamics, the present numerical study focuses on the representative case at fixed $\mathrm{Oh} = 2.8 \times 10^{-2}$ and $\omega_0 = 3.0$.

III. SPINNING-AFFECTED BOUNCING UPON HEAD-ON COLLISION

A. Spinning-induced off-center bouncing ($\varphi = \pi/2$)

The head-on collision between a spinning D1 and a nonspinning D2 at $\mathrm{We} = 9.3$ and $\mathrm{Oh} = 2.8 \times 10^{-2}$ is shown in Fig. 5(b). The head-on collision between two nonspinning droplets is shown in Fig. 5(a) for comparison. The representative case with $\varphi = \pi/2$ has been concerned first, and thereby the spinning angular velocity for D1 is given by $\boldsymbol{\omega}_0 = -\omega_0\boldsymbol{j}$. Due to the symmetry breaking by the spinning motion, three-dimensional flow features appear in the results, and they are illustrated on both the symmetry (x-z) plane and the yO_1O_2 plane, where the y axis and $\overline{O_1O_2}$ lie, as shown in Fig. 5(b). For the nonspinning case, the axis-symmetric results are illustrated on the symmetry (x-z) plane, as shown in Fig. 5(a).

Some similarities are observed for these two cases in terms of the evolution of droplet deformation. The droplet interaction results in the locally enhanced capillary pressure around the rim of the interaction region where local curvature is large. The maximum droplet deformation is reached at about $T = 0.35$. The deformed droplets bounce back (at about $T = 0.90$) driven by the surface tension force, meanwhile converting the surface energy back to the kinetic energy. Subsequently, the droplets experience several oscillation periods before completely

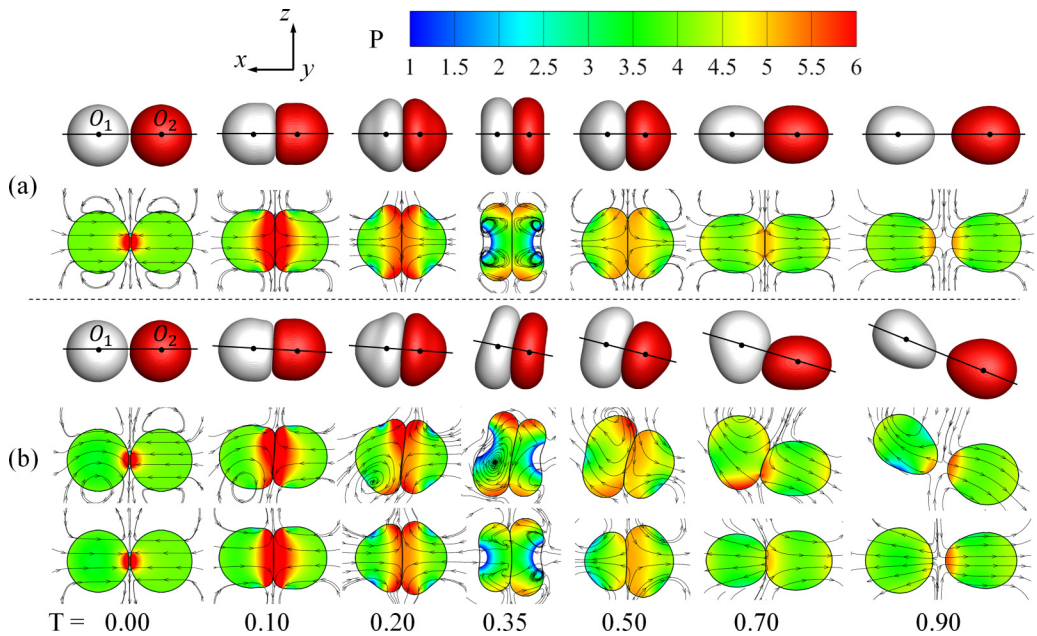

FIG. 5. Comparison of deformation, pressure profiles, and streamlines for the head-on droplet collision: (a) two nonspinning droplets and (b) a spinning droplet 1 ($\boldsymbol{\omega}_0 = -\omega_0 \boldsymbol{j}$) with a nonspinning droplet 2. The results are shown on the x-z plane only for cases (a) because they are axisymmetric, but both on the x-z plane at the first two rows and on the plane yO_1O_2 consisting of the y axis and $\overline{O_1O_2}$ at the last row for case (b).

recovering their initial spherical shapes, which happens at later times beyond those shown in Fig. 5.

A prominent difference can be seen for the two cases. Compared with the nonspinning case in Fig. 5(a), the nonaxisymmetric droplet deformation with $\overline{O_1O_2}$ deviated from the x axis is observed in Fig. 5(b). This is attributed to the existence of interchanges between $\boldsymbol{L}_\mathrm{t}$, $\boldsymbol{L}_\mathrm{o}$, and $\boldsymbol{L}_\mathrm{s}$, as shown in Fig. 6. Specifically, $\boldsymbol{L}_{\mathrm{s}1}$ (initially equal to $\boldsymbol{L}_\mathrm{t}$) causes a small increase of $\boldsymbol{L}_{\mathrm{s}2}$ and a prominent increase of $\boldsymbol{L}_\mathrm{o}$. This implies that the spinning motion of D1 can slightly rotate the nonspinning D2 but induces a prominent nonaxisymmetric flow even by means of a head-on collision. For the present bouncing cases, the interchange of $\boldsymbol{L}_\mathrm{s}$ and $\boldsymbol{L}_\mathrm{o}$ can be realized only by means of the intervening gas film between the droplets.

To illustrate the role of the gas film in affecting the interchange of angular momentum, we show the vorticity amplitude $|\boldsymbol{\omega}|$ and the velocity vector in Fig. 7. The vorticity in the spinning D1 is prominently larger than that in the nonspinning D2. For the head-on collision between two nonspinning droplets, the gas film and the internal flow in the lubrication layer are approximately parallel to the collision plane; for the head-on collision between the spinning D1 and the nonspinning D2, the gas film is curved with its thickness varying prominently along the lubrication layer. As seen in a closeup of the gas film region, shown in Fig. 7(b), the velocity vector of internal flow among the lubrication layer forms an angle with the gas film so that the shear flow in D1 can induce a shear flow in D2.

B. Influence of the orientation of spinning axis ($\varphi \neq \pi/2$)

Apart from the special case with $\varphi = \pi/2$, the more general cases with varying spinning axes at $\varphi = 0,\ \pi/6, \pi/4$, and $\pi/3$ were studied to reveal the angular momentum interchange between two droplets. It is seen that L_t in each direction is conserved at time instants of $T = 0.0$ and

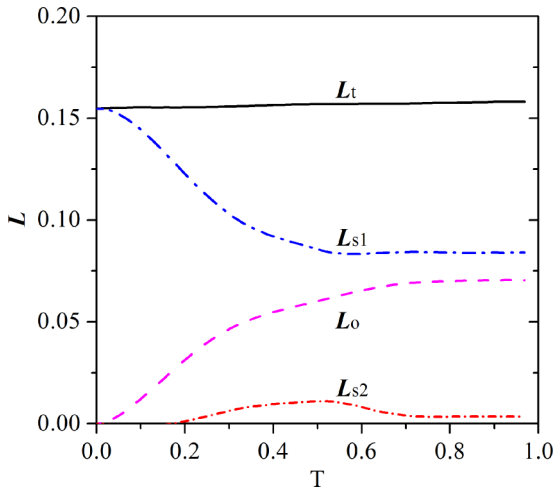

FIG. 6. Interchange between spinning angular momentum, $\boldsymbol{L}_{s1}$ and $\boldsymbol{L}_{s2}$, and orbital angular momentum, $\boldsymbol{L}_{o}$, for the head-on collision between a spinning droplet 1 and a nonspinning droplet 2 shown in Fig. 5(b).

$T = 1.0$, as shown in Fig. 8, and only L_{s1} presents at $T = 0.0$ because of the initial head-on collision.

The most significant nonaxisymmetric flow due to the spinning effects occurs in the direction parallel to the x-z plane, as indicated by the prominent L_o after the droplet collision, shown in Fig. 8(b). Specifically, for L_y shown in Fig. 8(b), the initial L_{s1} increases with increasing φ; regardless of the negligible L_{s2}, the L_o after the droplet collision reaches a maximum value at $\varphi = \pi/2$, whereas for L_x and L_z shown in Figs. 8(a) and 8(c), a very small L_o is observed at $T = 1.0$, implying that the interaction between D1 and D2 is too weak (on the y-z plane and x-y plane) to cause the apparent nonaxisymmetric flow. This finding suggests that the orthogonality

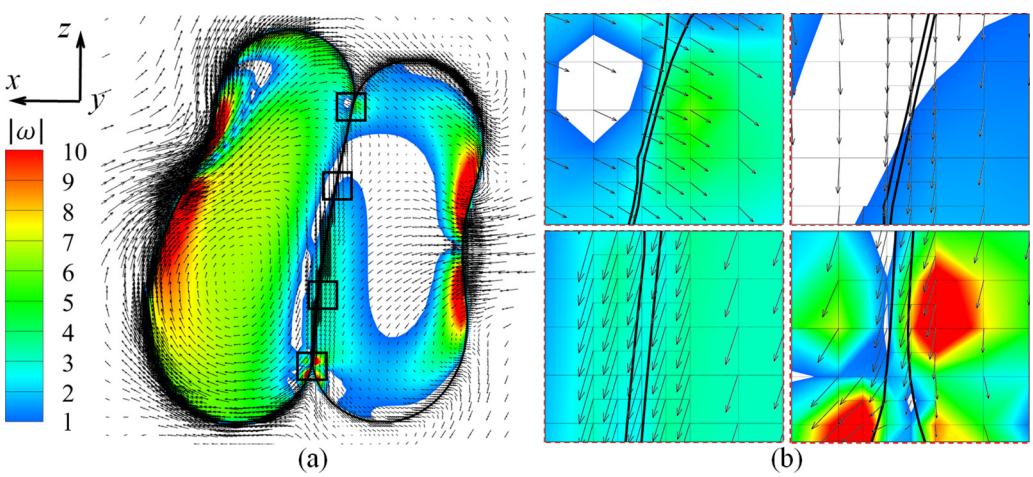

FIG. 7. Effects of gas film on the internal flow by the spinning motion of droplets shown in Fig. 5(b): (a) vorticity magnitude $|\boldsymbol{\omega}|$ and velocity vector on the symmetry x-z plane and (b) closeup of the gas film regions. The white region inner droplets denote $|\boldsymbol{\omega}|$ less than 1.0, which has been blanked for clear comparison of the vorticity concentration.

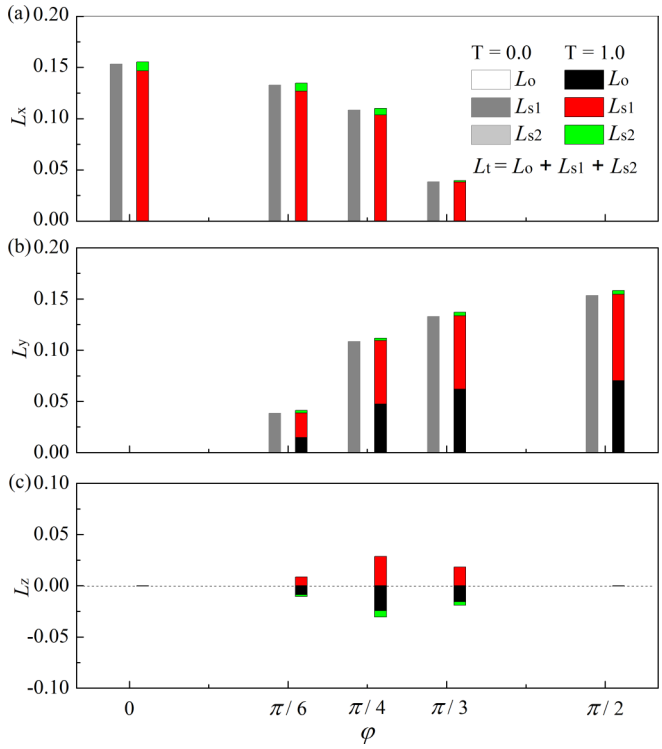

FIG. 8. Comparison of spinning angular momentum, L_{s1} and L_{s2}, and orbital angular momentum, L_o, at time instants of $T = 0.0$ and $T = 1.0$ with varying the azimuthal angle φ. (a) L_x, (b) L_y, and (c) L_z are the angular momentum in x, y, and z directions, respectively.

of the initial translational motion of two droplets and the spinning motion of D1 is important for generating the nonaxisymmetric flow.

C. Roles of rotational kinetic energy

To further investigate the interchange among different forms of energy, the energy budget is analyzed for the spinning D1 and nonspinning D2 separately, excluding the negligible energy in the gas phase [37]. The initial total energy (TE_0) of D1 is defined as $TE_0 = SE_0 + TKE_0 + RKE_0$, with the surface energy $SE_0 = \pi$, the translational kinetic energy $TKE_0 = \pi We/48$, and the rotational kinetic energy $RKE_0 = {\omega_0}^2\pi/120$. The initial total energy of D2 is $TE_0 = SE_0 + TKE_0$.

It is seen that the $TE = SE + TKE + RKE + TVDE$ in Fig. 9 is approximately constant during the entire collision process, justifying again the neglect of the energy budget in the gas phase. Here the total viscous dissipation energy (TVDE) is defined as

$$\mathrm{TVDE(T)} = \int_0^{\mathrm{T}} \left(\int_V H(c_1 + c_2 - 1)\phi dV \right) d\mathrm{T}, \tag{8}$$

where ϕ is the local viscous dissipation rate (VDR) given by

$$\phi = 2\mu\left[\left(\frac{\partial u}{\partial x}\right)^2 + \left(\frac{\partial v}{\partial y}\right)^2 + \left(\frac{\partial w}{\partial z}\right)^2\right] + \mu\left[\left(\frac{\partial u}{\partial y} + \frac{\partial v}{\partial x}\right)^2 + \left(\frac{\partial v}{\partial z} + \frac{\partial w}{\partial y}\right)^2 + \left(\frac{\partial w}{\partial x} + \frac{\partial u}{\partial z}\right)^2\right]. \tag{9}$$

However, the separated TE_1 and TE_2 show that the energy is transferred from D2 to D1 with φ smaller than $\pi/4$ while being transferred from D1 to D2 with φ larger than $\pi/4$. The energy

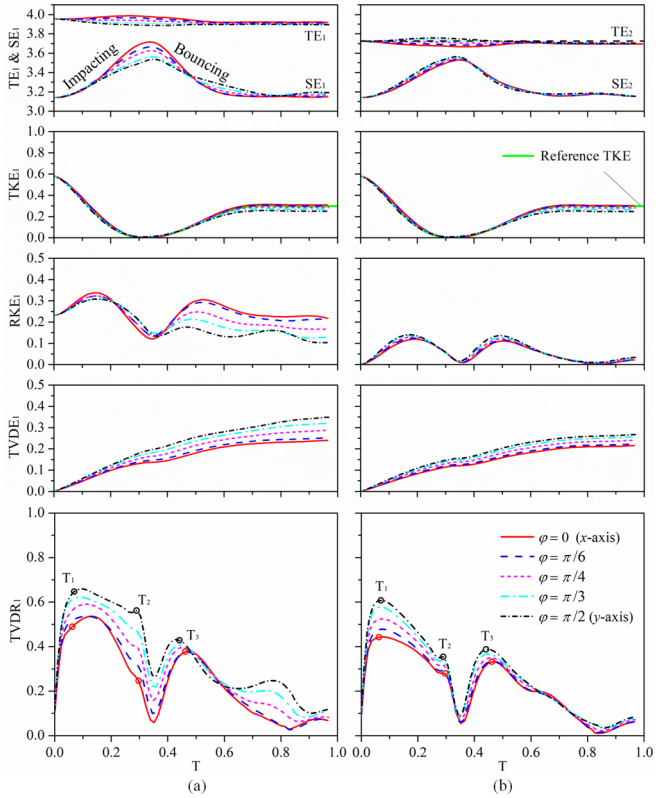

FIG. 9. Energy budget of head-on collisions between (a) a spinning droplet 1 and (b) a nonspinning droplet 2 with varying the azimuthal angle φ shown in Fig. 8. The total energy (TE), the surface energy (SE), the translational kinetic energy (TKE), the rotational kinetic energy (RKE), the total viscous dissipation energy (TVDE), and the total viscous dissipation rate (TVDR) are nondimensionalized for each liquid droplet separately. The reference TKE is for the collision between two nonspinning droplets.

interchange between D1 and D2 must occur by means of the KE. Compared with the reference TKE in Fig. 9 of the head-on collision between two nonspinning droplets, the spinning effects of D1 have insignificant influences on the evolution of TKE, with the curves of TKE_1 and TKE_2 collapsing with each other in the early stage and showing slight differences in the later stage. It is thereby inferred that the RKE plays a dominant role in the energy interchange between D1 and D2, with an apparent viscous loss of RKE_1 at $\varphi = \pi/2$, as indicated by the $TVDE_1$ curve shown in Fig. 9(a).

The viscous dissipation varies monotonically with φ for the representative case at $We = 9.3$ and $Oh = 2.8 \times 10^{-2}$. At $\varphi = 0$, as shown in Fig. 10(b), apart from the inertial force responsible for the droplet radial spreading, the centrifugal force by the spinning motion of D1 is also in the radial direction and can further promote the radial spreading. Consequently, the VDR distribution in Fig. 10(b) is similar to that of the nonspinning case in Fig. 10(a). At $\varphi = \pi/2$, the substantial $TVDE_1$ can be explained as the strong interaction between the rotating flow parallel to the x-z plane owing to the spinning motion of D1 and the radial flow induced by the collision between D1 and D2. This interaction occurs mainly on the x-z plane and forms an intense nonaxisymmetric flow, as indicated by the VDR concentration on the x-z plane shown in Fig. 10(c). Consequently, we can conclude that the rotational kinetic energy loss is responsible for the nonaxisymmetric flow by the interaction between the rotating and radial flows.

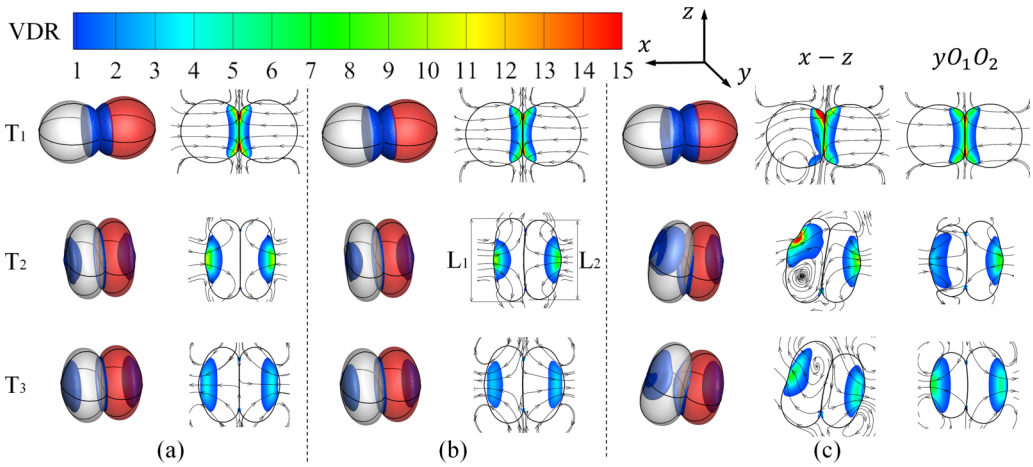

FIG. 10. Contour of the local viscous dissipation rate (VDR) and streamlines for the cases at three chosen time instants, T_1, T_2, and T_3, shown in Fig. 9, with (a) the collision between two nonspinning droplets at same time instants, (b) $\varphi = 0$, and (c) $\varphi = \pi/2$. The contours have been blanked with a low threshold value of 0.5 for clear comparison of the VDR concentration.

IV. SPINNING-AFFECTED COALESCENCE UPON HEAD-ON COLLISION

A. Nonaxisymmetric droplet deformation and delayed separation

Only the azimuth angle $\varphi = \pi/2$ is considered in this section to study the spinning effects on the collision-induced coalescence, because the preceding section has suggested that the interaction between the rotating flow and the radial flow tends to be maximal at $\varphi = \pi/2$. Furthermore, it should be emphasized that we aim to focus on studying the spinning effects on droplet coalescence by consistent numerical comparison through the same numerical setup and mesh parameters expatiated in Sec. II. We do not intend to study the spinning effects on gas film drainage and on the interface rupture, which indeed merits future study but cannot be considered in the present computational framework.

As shown in Fig. 11, the merged droplet reaches its maximum deformation by depleting all kinetic energy; then it contracts from a "disk" to a "filament" and finally leads to separation with a satellite droplet. The symmetric separation in Fig. 11(a) occurs at about $T = 1.74$, while the nonsymmetric separation in Fig. 11(b) is delayed to about $T = 1.81$. Furthermore, the liquid filament on the side of D2 is pinched off earlier than the other side of D1, leading to the formed satellite droplet being closer to D1, which is attributed to the nonaxisymmetric flow induced by the spinning motion of D1.

In the previous studies [4,5,18] a delayed or suppressed separation is usually attributed to the enhanced internal-flow-induced viscous dissipation with increasing liquid viscosity or droplet interminglement duration. The delayed separation in the present problem is also affected by the enhanced viscous dissipation, but it is owing to the interaction between the rotating flow and the radial flow. This can be verified by the local VDR and streamlines shown in Fig. 12. Specifically, as the droplet contracts from a "disk" to a "filament," Figs. 12(a) and 12(b) show nearly the same filament length at $T = 0.82$. However, as shown by the red arrows, case (b) has a larger filament width on the x-z plane while having a smaller filament width on the specific planes denoted by a series of solid lines. The nonaxisymmetric droplet deformation would promote the interface oscillation and cause enhanced internal-flow-induced viscous dissipation, as the enhanced VDR in the vicinity of the oscillating interface on the x-z plane shown at $T = 1.27$. Consequently, the viscous dissipation accompanied by the nonaxisymmetric interface oscillation leads to the filament

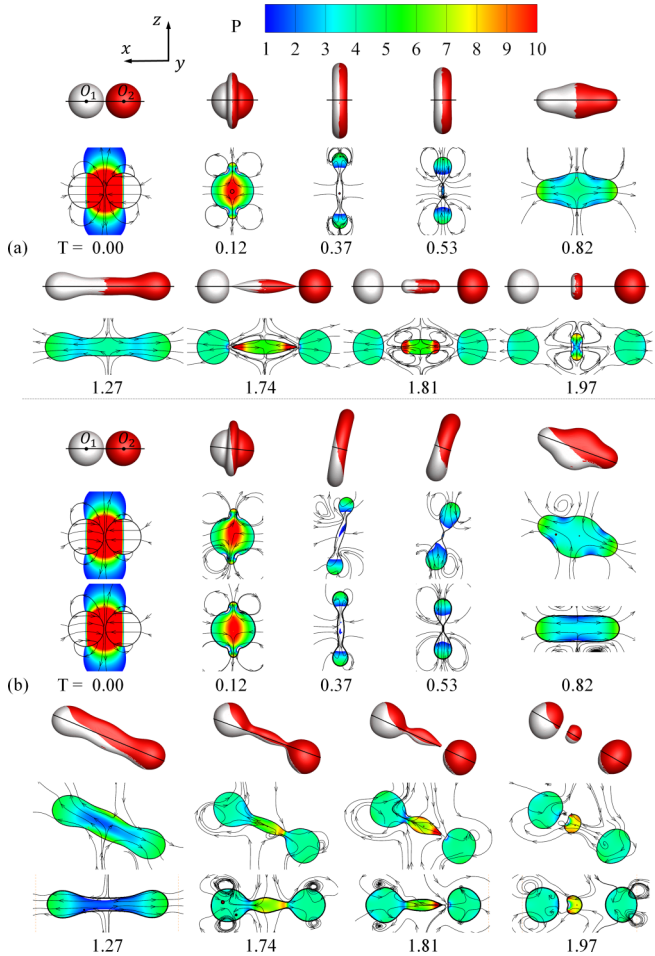

FIG. 11. Comparison of deformation, pressure profiles, and streamlines for the droplet coalescence and subsequent separation at We = 61.4 and Oh = 2.8×10^{-2}: (a) two nonspinning droplets and (b) a spinning droplet 1 ($\boldsymbol{\omega}_0 = -\omega_0 \boldsymbol{j}$) with a nonspinning droplet 2. The third line of case (b) is the contour on the plane that is parallel to the y axis and illustrated by solid lines.

length of case (b) being prominently shorter than that of case (a) at $T = 1.27$ and 1.74, so that the droplet in case (b) requires more time to separate.

B. Enhanced internal mass interminglement by spinning effects

It is also interesting to note that, in Fig. 11, regardless of the satellite droplet containing the liquid mass from both D1 and D2, mass exchange between D1 and D2 can be observed for the spinning case but not in the nonspinning case, which implies that the spinning effects can promote the internal mass interminglement by breaking the mirror symmetry between two identical droplets.

To quantitatively characterize the mass interminglement between D1 and D2, the temporal area changes of the colored contact surface of the droplet were numerically calculated and shown in Fig. 13. The contact surface area $A(t)$ of the droplet is normalized by the initial surface area A_0 of the droplets. Because the mesh resolutions on the gas-liquid interface and inside the droplet are fixed in the present simulation setup, the normalized colored contact surface area $A(t)/A_0$ can be

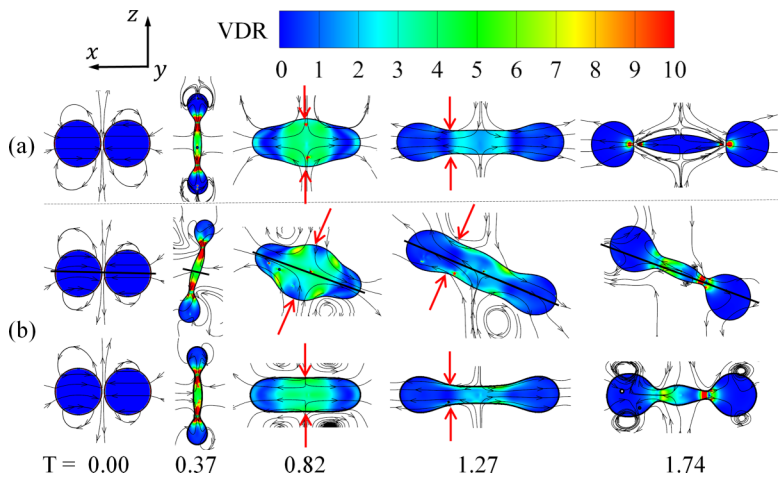

FIG. 12. Local viscous dissipation rate (VDR) and streamlines for the coalescence shown in Fig. 11: (a) two nonspinning droplets and (b) a spinning droplet 1 with a nonspinning droplet 2. The legend of VDR is divided by 5 for $T = 0.82$ and $T = 1.27$.

approximately calculated by [20]

$$\frac{A(t)}{A_0} = \frac{N[0 < \phi(t) < 1]H[c(t) - 1]}{N[0 < c(0) < 1]}, \tag{10}$$

where N is the number of the meshes in which the VOF function $c(t)$ or the mass dye (color) function $\phi(t)$ take certain values within their ranges and thus can be treated as functionals of $c(t)$ or $\phi(t)$. The color function $\phi(t) = 1$ denotes the spinning D1, $0 < \phi(t) < 1$ the contact surface of the droplets, and $\phi(t) = 0$ the nonspinning D2. Again, the Heaviside step function ensures only those meshes within the droplet are counted in the calculation. It should be noted that the mass

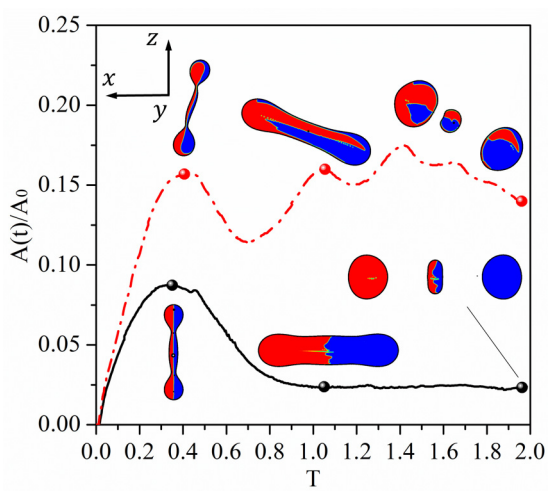

FIG. 13. Evolution of temporal contact surface area $A(t)/A_0$ to characterize the mass interminglement between the droplets shown in Fig. 11, with a solid line for two nonspinning droplets and a dashed dot line for a spinning droplet 1 with a nonspinning droplet 2.

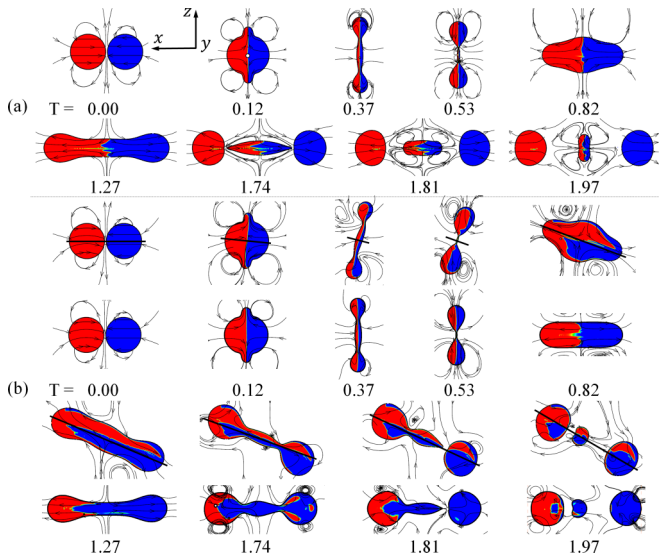

FIG. 14. Internal mass interminglement for (a) two nonspinning droplets and (b) a spinning droplet 1 (left) with a nonspinning droplet 2 (right) shown in Fig. 11.

interminglement concerned in the present study is not the physical mixing, and $A(t)/A_0$ is calculated by the numerical dyer function without liquid diffusion effects. The results show that the spinning motion of D1 can lead to prominent increase of $A(t)/A_0$, because the colored contact surface is stretched along the filament owing to the nonaxisymmetric flow, as illustrated by the embedded internal mass interminglement on the x-z plane shown in Fig. 13.

Figure 14 shows the entire process of the enhanced mass interminglement and internal liquid mass stretching along the filament by the spinning effects. Specifically, as the mass interminglement shown at $T = 0.12$ and 0.37 in Fig. 14(b), the liquid mass from D1 by spinning effects would pass through the mirror symmetry plane of the head-on collision of equal-size droplets composed of the same liquid and lead to locally nonuniform mass distribution around the rim of the interaction region. In the meantime, the colored contact surface inside the merged droplet is rotated and deviated from the x-y plane. Then the merged droplet with nonuniform mass distribution begins to contract from the inclined "disklike" deformation to an inclined filament, as the contour at $T = 0.53$ and 0.82 on the x-z plane shows in Fig. 14(b), and is further stretched along the filament in the subsequent droplet deformation. It is noted that the mass interminglement on the specific planes, which are parallel to the y axis and denoted by a series of solid lines in Fig. 11, still holds the mirror symmetry with respect to the x-z plane. Consequently, it can be understood that the nonaxisymmetric flow induced by the spinning effects at the early impacting stage would be enlarged in a later droplet deformation stage and lead to the enhanced mass interminglement.

V. CONCLUDING REMARKS

A computational study of the head-on bouncing and coalescence between a spinning droplet and a nonspinning droplet was investigated based on a validated volume-of-fluid method. The most interesting discovery is that the spinning motion has a significant role in affecting both droplet bounce and coalescence.

For the head-on droplet bouncing, the spinning motion of droplets can induce nonaxisymmetric flow features, because a part of the initial spinning angular momentum is converted into the orbital angular momentum. With varying the spinning axis of the droplet, the nonaxisymmetric flow becomes the most significant when the spinning axis is perpendicular to the direction of relative

velocity. This indicates that the orthogonality of the initial translational motion of two droplets and the spinning motion of droplets are important factors related to enhancing the nonaxisymmetric flow. In the aspects of energy conversion, the translational kinetic energy after droplet bouncing is not sensitive to the variation of spinning axis, whereas the apparent rotational kinetic energy loss to the viscous dissipation is attributed to the interaction between the rotating flow induced by droplet spinning motion and the radial flow induced by the droplet's translational impacting motion.

For the head-on droplet coalescence, the spinning motion of the droplet leads to a delayed separation after temporary coalescence, compared with the case between two nonspinning droplets. The delayed coalescence is attributed to the enhanced interface oscillation and internal-flow-induced viscous dissipation due to the nonaxisymmetric droplet deformation. Furthermore, the spinning effects can significantly promote the mass interminglement by breaking the mirror symmetry of the head-on collision of equal-size droplets composed of the same liquid. This is because the nonaxisymmetric flow by the spinning effects leads to locally nonuniform mass interminglement at the early collision stage, and because the contact interface between the mass from different droplets is further stretched along the filament in the later collision stages.

The primary objective of this work is to substantiate the mechanism of droplet spinning in droplet collision, which was overlooked in previous studies. It should be noted that although the present study deliberately limits its scope to the spinning effects on the collision between a spinning droplet and a nonspinning droplet, the discovered phenomena are believed to exist in general and may be more substantial in appropriate collision situations. A complete parametric study is certainly merited in future work. However, the spinning effects on the droplet collision in practical situations are more complex, because quite a few spinning-related parameters (for example, the intensity of droplet spinning speed, three Euler angles, and chirality) are needed to completely characterize a spinning droplet. Last but not the least, the experimental confirmation of the present results may be of interest but certainly require innovation of the current experimental techniques in generating and controlling spinning droplets.

ACKNOWLEDGMENTS

This work was supported partly by the Hong Kong RGC/GRF (through Grant No. PolyU 152188/20E) and partly by the Hong Kong Polytechnic University (through Grants No. G-SB1Q and No. G-YBXN).

[1] P. R. Brazier-Smith, S. G. Jennings, and J. Latham, The interaction of falling water drops: Coalescence, Proc. R. Soc. London, Ser. A **326**, 393 (1972).

[2] S. G. Bradley and C. D. Stow, Collisions between liquid drops, Proc. R. Soc. A **287**, 635 (1978).

[3] N. Ashgriz and J. Y. Poo, Coalescence and separation in binary collisions of liquid drops, J. Fluid Mech. **221**, 183 (1990).

[4] Y. J. Jiang, A. Umemura, and C. K. Law, An experimental investigation on the collision behavior of hydrocarbon droplets, J. Fluid Mech. **234**, 171 (1992).

[5] J. Qian and C. K. Law, Regimes of coalescence and separation in droplet collision, J. Fluid Mech. **331**, 59 (1997).

[6] J.-P. Estrade, H. Carentz, G. Lavergne, and Y. Biscos, Experimental investigation of dynamic binary collision of ethanol droplets—A model for droplet coalescence and bouncing, Int. J. Heat Fluid Flow **20**, 486 (1999).

[7] M. Sommerfeld and M. Kuschel, Modelling droplet collision outcomes for different substances and viscosities, Exp. Fluids **57**, 187 (2016).

[8] G. Finotello, R. F. Kooiman, J. T. Padding, K. A. Buist, A. Jongsma, F. Innings, and J. Kuipers, The dynamics of milk droplet–droplet collisions, Exp. Fluids **59**, 17 (2018).

[9] K. H. Al-Dirawi and A. E. Bayly, A new model for the bouncing regime boundary in binary droplet collisions, Phys. Fluids **31**, 027105 (2019).
[10] K.-L. Pan, C. K. Law, and B. Zhou, Experimental and mechanistic description of merging and bouncing in head-on binary droplet collision, J. Appl. Phys. **103**, 064901 (2008).
[11] G. Brenn, Droplet collision, in *Handbook of Atomization and Sprays*, edited by N. Ashgriz (Springer, Berlin, 2011), p. 157.
[12] H. P. Kavehpour, Coalescence of drops, Annu. Rev. Fluid Mech. **47**, 245 (2015).
[13] M. Orme, Experiments on droplet collisions, bounce, coalescence and disruption, Prog. Energy Combust. Sci. **23**, 65 (1997).
[14] K.-L. Pan, P.-C. Chou, and Y.-J. Tseng, Binary droplet collision at high Weber number, Phys. Rev. E **80**, 036301 (2009).
[15] N. Roth, C. Rabe, B. Weigand, F. Feuillebois, and J. Malet, Droplet collision outcomes at high Weber number, in *Proc. of the 21st Conf. of the Institute for Liquid Atomization and Spray Systems* (ILASS, Mugla, Turkey, 2007).
[16] G. Finotello, J. T. Padding, N. G. Deen, A. Jongsma, F. Innings, and J. Kuipers, Effect of viscosity on droplet-droplet collisional interaction, Phys. Fluids **29**, 067102 (2017).
[17] C. Gotaas, P. Havelka, H. A. Jakobsen, H. F. Svendsen, M. Hase, N. Roth, and B. Weigand, Effect of viscosity on droplet-droplet collision outcome: Experimental study and numerical comparison, Phys. Fluids **19**, 102106 (2007).
[18] C. Tang, P. Zhang, and C. K. Law, Bouncing, coalescence, and separation in head-on collision of unequal-size droplets, Phys. Fluids **24**, 022101 (2012).
[19] C. Tang, J. Zhao, P. Zhang, C. K. Law, and Z. Huang, Dynamics of internal jets in the merging of two droplets of unequal sizes, J. Fluid Mech. **795**, 671 (2016).
[20] D. Zhang, C. He, P. Zhang, and C. Tang, Mass interminglement and hypergolic ignition of TMEDA and WFNA droplets by off-center collision, Combust. Flame **197**, 276 (2018).
[21] Z. Zhang, Y. Chi, L. Shang, P. Zhang, and Z. Zhao, On the role of droplet bouncing in modeling impinging sprays under elevated pressures, Int. J. Heat Mass Transf. **102**, 657 (2016).
[22] Z. Zhang and P. Zhang, Cross-impingement and combustion of sprays in high-pressure chamber and opposed-piston compression ignition engine, Appl. Therm. Eng. **144**, 137 (2018).
[23] Z. Zhang and P. Zhang, Modeling kinetic energy dissipation of bouncing droplets for Lagrangian simulation of impinging sprays under high ambient pressure, Atom. Sprays **28**, 673 (2018).
[24] P. J. O'Rourke and F. V. Bracco, Modeling of drop interactions in thick sprays and a comparison with experiments, Stratified Charge Automated Engineering Conference, Inst. Mech. Engng. **9**, 101 (1980).
[25] S. L. Post and J. Abraham, Modeling the outcome of drop–drop collisions in diesel sprays, Int. J. Multiphase Flow **28**, 997 (2002).
[26] R. A. Brown and L. E. Scriven, The shape and stability of rotating liquid drops, Proc. R. Soc. London, Ser. A **371**, 331 (1980).
[27] H. Kitahata, R. Tanaka, Y. Koyano, S. Matsumoto, K. Nishinari, T. Watanabe, K. Hasegawa, T. Kanagawa, A. Kaneko, and Y. Abe, Oscillation of a rotating levitated droplet: Analysis with a mechanical model, Phys. Rev. E **92**, 062904 (2015).
[28] J. Holgate and M. Coppins, Shapes, stability, and hysteresis of rotating and charged axisymmetric drops in a vacuum, Phys. Fluids **30**, 064107 (2018).
[29] E. K. Poon, J. Lou, S. Quan, and A. S. Ooi, Effects of streamwise rotation on the dynamics of a droplet, Phys. Fluids **24**, 082107 (2012).
[30] B. Maneshian, K. Javadi, M. T. Rahni, and R. Miller, Droplet dynamics in rotating flows, Adv. Colloid Interface Sci. **236**, 63 (2016).
[31] E. Janiaud, F. Elias, J. Bacri, V. Cabuil, and R. Perzynski, Spinning ferrofluid microscopic droplets, Magnetohydrodynamics **36**, 301 (2000).
[32] S. Popinet, An accurate adaptive solver for surface-tension-driven interfacial flows, J. Comput. Phys. **228**, 5838 (2009).
[33] S. Popinet, Numerical models of surface tension, Annu. Rev. Fluid Mech. **50**, 49 (2018).

[34] X. Chen, D. Ma, P. Khare, and V. Yang, Energy and mass transfer during binary droplet collision, in *49th AIAA Aerospace Sciences Meeting* (AIAA, Reston, VA, 2011).
[35] X. Chen, D. Ma, and V. Yang, Collision outcome and mass transfer of unequal-sized droplet collision, in *50th AIAA Aerospace Sciences Meeting* (AIAA, Reston, VA, 2012).
[36] X. Chen and V. Yang, Thickness-based adaptive mesh refinement methods for multi-phase flow simulations with thin regions, J. Comput. Phys. **269**, 22 (2014).
[37] C. He, X. Xia, and P. Zhang, Non-monotonic viscous dissipation of bouncing droplets undergoing off-center collision, Phys. Fluids **31**, 052004 (2019).
[38] C. Hu, S. Xia, C. Li, and G. Wu, Three-dimensional numerical investigation and modeling of binary alumina droplet collisions, Int. J. Heat Mass Transf. **113**, 569 (2017).
[39] X. Xia, C. He, D. Yu, J. Zhao, and P. Zhang, Vortex-ring-induced internal mixing upon the coalescence of initially stationary droplets, Phys. Rev. Fluids **2**, 113607 (2017).
[40] X. Xia, C. He, and P. Zhang, Universality in the viscous-to-inertial coalescence of liquid droplets, PNAS **116**, 23467 (2019).
[41] P. Zhang and C. K. Law, An analysis of head-on droplet collision with large deformation in gaseous medium, Phys. Fluids **23**, 042102 (2011).
[42] E. Coyajee and B. J. Boersma, Numerical simulation of drop impact on a liquid–liquid interface with a multiple marker front-capturing method, J. Comput. Phys. **228**, 4444 (2009).
[43] C. He, X. Xia, and P. Zhang, Vortex-dynamical implications of nonmonotonic viscous dissipation of off-center droplet bouncing, Phys. Fluids **32**, 032004 (2020).